Enhanced d-p Orbital Hybridization Accelerates Two-Step Quasi-Solid-State Sulfur Conversion in Sodium-Sulfur Batteries

Mingyue Wang[1,3]†, Yubing Hu[4]†, Rui Li[5], Xinran Gao[1,3], Yameng Fan[3], Bernt Johannessen[3,6], Yaojie Lei[2], Shixue Dou[1,3], Nana Wang*[2,3], Langli Luo*[4], Guoxiu Wang[2], Zhongchao Bai*[1]

1. Institute of Energy Materials Science, University of Shanghai for Science and Technology, 516 Jungong Road, Shanghai 200093, China

2. Centre for Clean Energy Technology, School of Mathematical and Physical Sciences, Faculty of Science, University of Technology Sydney, Sydney, NSW, 2007 Australia

3. Institute for Superconducting and Electronic Materials, University of Wollongong, North Wollongong, NSW 2500, Australia

4. Institute of Molecular Plus, Department of Chemistry, Tianjin University, Tianjin 300072, China

5. Institute of Materials Research, Tsinghua Shenzhen International Graduate School, Tsinghua University, Shenzhen 518055, China

6. Australian Synchrotron, ANSTO, 800 Blackburn Road, Clayton, Victoria 3168, Australia

*Corresponding authors. Email: Nana.Wang@uts.edu.au; luolangli@tju.edu.cn; baizhongchao@tyut.edu.cn.

Experimental section

Fabrication of Mo_2C/C

First, the carbon spheres (C) were synthesized following a previously reported method as host.[1] Then, Bis(acetylacetonato)dioxomolybdenum(VI) as the molybdenum precursor was mixed with C at a 1:1 mass ratio. The mixture was calcined in a tube furnace at 700 °C for 8 hours under a H_2/Ar (5% H_2) atmosphere, with a heating rate of 2 °C min^{-1}.

Fabrication of S@Mo_2C/C and S@C

Mo_2C/C and C were mixed with sulfur powder in a 1:3 mass ratio and thoroughly

ground in an agate mortar. The resulting mixture was sealed in an ampoule, placed within a quartz tube, and subjected to heating at 155 °C for 12 hours. Afterward, the temperature ramped up to 300 °C at a rate of 5 °C min^{-1} and held steady for 2 h.

Materials characterizations

The morphological characterization was conducted using a field emission scanning electron microscope (FESEM, JEOL JSM-7500FA, JSM-7600F). High-resolution transmission electron microscopy (HRTEM) images, selected area electron diffraction (SAED) patterns, and high-angle annular dark field scanning transmission electron microscopy (HAADF-STEM) images, along with energy dispersive spectroscopy (EDS) elemental mappings, were obtained using a Thermo Scientific™ Talos F200X. X-ray diffraction (XRD) patterns were recorded with a PANalytical Empyrean system equipped with Cu Kα radiation. X-ray photoelectron spectroscopy (XPS) measurements were carried out using a Thermo Scientific Nexsa spectrometer. Thermogravimetric analysis (TGA) was performed with a NETZSCH TGA 209 analyzer to evaluate the thermal decomposition properties of the samples from 25 °C to 800 °C at a heating rate of 10 °C min^{-1}. X-ray absorption spectroscopy (XAS) data were collected at the XAS and medium energy (MEX-2) beamlines at the Australian Synchrotron, ANSTO. *In situ* electrochemical atomic force microscopy (EC-AFM) imaging was achieved using a Bruker Bioscope Resolve AFM system. The *in situ* electrochemical setup featured a three-electrode configuration, with a Na pole serving as the counter electrode and reference electrode, and the S@Mo_2C/C or S@C electrode functioning as the working electrode.

In situ TEM characterization

The Na-S@Mo_2C/C nanobattery was assembled within a FEI Talos F200X TEM using an *in situ* electrical probing TEM holder (ZepTools Co. Ltd., China). The process began in an Ar-filled glovebox, where the sample powder was adhered to the rough edge of a semi-molybdenum grid, serving as the working electrode. Sodium metal was then affixed to the tip of a tungsten (W) probe, functioning as the counter electrode. The W

probe, equipped with a piezo-motor for precise three-dimensional positioning and electrical bias control, facilitated the assembly process. The TEM holder, enclosed in an Ar-filled zip-lock bag, was subsequently transferred to the TEM column. Brief exposure of the Na metal to air (<5 seconds) intentionally formed a Na_2O solid-state electrolyte layer on its surface, enabling conductive Na-ion transport. Upon establishing contact between the sample and the Na_2O/Na layer, a constant bias voltage was applied to the W probe, thereby completing the *in situ* assembly of the Na-S@Mo_2C/C nanobattery system.

Electrochemical measurements

The active material, Super P, and carboxymethyl cellulose (CMC) binder were combined in a mass ratio of 7:2:1, with water gradually added to create a homogeneous slurry. This slurry was uniformly applied to copper foil using a doctor blade and dried in a vacuum oven at 50 °C for 12 hours. CR2032 coin cells were fabricated in an argon-filled glovebox for evaluating the electrochemical performance of the Na-S system. Na metal was used as the anode, glass fiber (Whatman GF/D) as the separator, and the electrolyte consisted of 1 M $NaClO_4$ dissolved in a solution of propylene carbonate (PC) and ethylene carbonate (EC) (1:1 by volume) with 5 wt% fluoroethylene carbonate (FEC) additive. All reported capacities are calculated based on the mass of sulfur. The sulfur loading of the electrodes used for the ultrahigh-rate tests is approximately 0.5-0.8 mg cm^{-2} unless otherwise specified, with an electrolyte-to-sulfur (E/S) ratio of 40 μL mg^{-1}. In the supporting information, the sulfur loadings are explicitly specified as ~1.2 mg cm^{-2} and 3.0 mg cm^{-2} for the corresponding datasets. For the pouch cell, the S@Mo_2C/C cathode was cut into a 50 mm × 40 mm rectangle, and the sulfur loading is 1.2 mg cm^{-2}. Cycling stability and rate capability were tested on a LAND battery testing system at ambient temperature. Cyclic voltammetry (CV) and electrochemical impedance spectroscopy (EIS) analyses were carried out using a Bio-Logic VMP3 potentiostat. The CV measurements were conducted at a scan rate of 0.1 mV s^{-1}. Tafel plots were derived by fitting the linear region of the log (current density)-voltage plots before the appearance of the oxidation and reduction peaks. The EIS measurements

were carried out using a frequency range from 100 kHz to 10 Hz under open-circuit voltage conditions.

Computational methods

Spin-polarized density functional theory (DFT) calculations were carried out using the Vienna Ab initio Simulation Package (VASP).[2, 3] The interactions between ionic cores and valence electrons were described by the projector augmented-wave (PAW) method.[4] Exchange-correlation effects were treated within the generalized gradient approximation (GGA) using the Perdew-Burke-Ernzerhof (PBE) functional.[5, 6] A plane-wave kinetic energy cutoff of 450 eV was employed. The Monkhorst-Pack scheme with a k-point separate on length of 0.05 $Å^{-1}$ was utilized for sampling the first Brillion zone, setting as 3×3×1. A vacuum layer of 15 Å was introduced normally to the surface to eliminate spurious interactions between periodic images. All atomic structures were fully relaxed using the quasi-Newton algorithm until the total energy converged to within 1.0×10^{-5} eV and the residual force on each atom was less than 0.01 eV $Å^{-1}$.

Gibbs free energy profiles were constructed to evaluate the thermodynamics of the reaction pathway. The Gibbs free energy change (ΔG) for each elementary step was calculated based on the zero-point energy (ZPE)-corrected DFT total energy, which was taken as the enthalpy at 0 K, according to:

$$\Delta G = \Delta H - T\Delta S = \Delta E_{DFT} + \Delta E_{ZPE} + \int_{0}^{298.15K} \Delta C_V dT - T\Delta S$$

Where ΔE_{DFT} is the total energy difference obtained from DFT optimization, ΔE_{ZPE} is the zero-point vibrational energy correction, ΔC_V denotes the heat capacity difference, T is the kelvin temperature, and ΔS represents the entropy difference.

Projected density of states (PDOS) analysis was performed using the VASPKIT package based on the optimized structures.[7] The atom-pair-specific crystal orbital Hamilton population (COHP) analysis was performed using the LOBSTER program, which projects wave-functions (from PBE calculations) onto target atoms via Mulliken population analysis.

The fabrication process of the Mo_2C/C composite and the S@Mo_2C/C cathode is

schematically illustrated in **Fig. S1**. The cross-linked carbon spheres were synthesized following a previously reported strategy.[1] Briefly, uniform $MnCO_3$ microspheres were first obtained via a coprecipitation method (**Fig. S2**), and then calcined at 550 °C under an Ar atmosphere to yield porous Mn_2O_3 microspheres composed of interconnected nanoparticles (**Fig. S3**). These were subsequently annealed at 650 °C under an Ar atmosphere to produce MnO@C intermediates, which were then acid-etched with dilute HCl to remove the MnO core, resulting in a hierarchically porous, cross-linked carbon framework (**Fig. S4**). This hierarchical conductive architecture serves not only as a robust physical barrier to confine sulfur but also as a favorable matrix for uniformly anchoring catalytic sites. Bis(acetylacetonato)dioxomolybdenum(VI) was used as the Mo precursor to synthesize ultrasmall Mo_2C nanoparticles via *in situ* pyrolysis. The resulting Mo_2C/C and S@Mo_2C/C composites retain the interconnected spherical morphology (**Fig. S5-S6**).

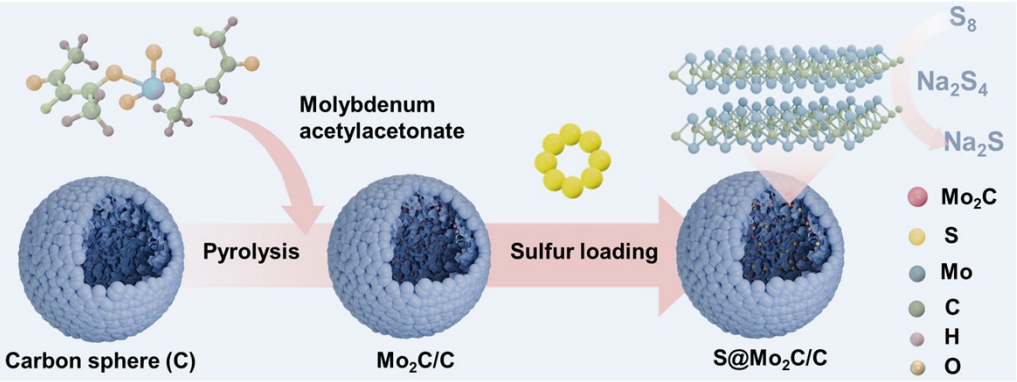

Figure S1. Schematic fabrication process and structure of S@Mo_2C/C composite and sulfur reduction process.

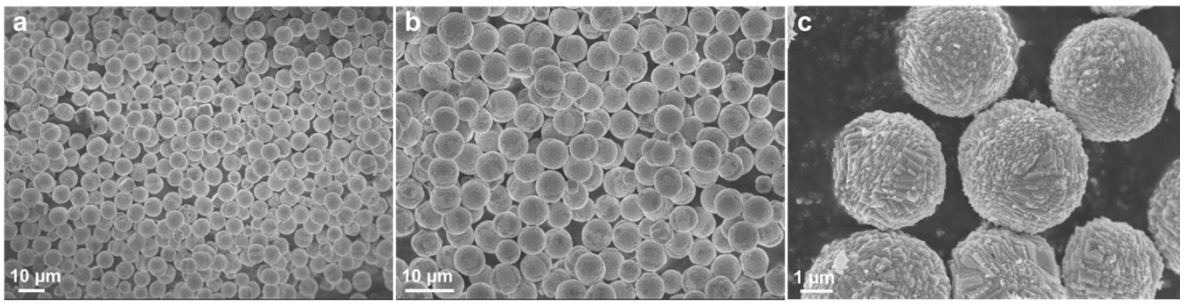

Figure S2. (a-c) SEM images of $MnCO_3$ sphere.

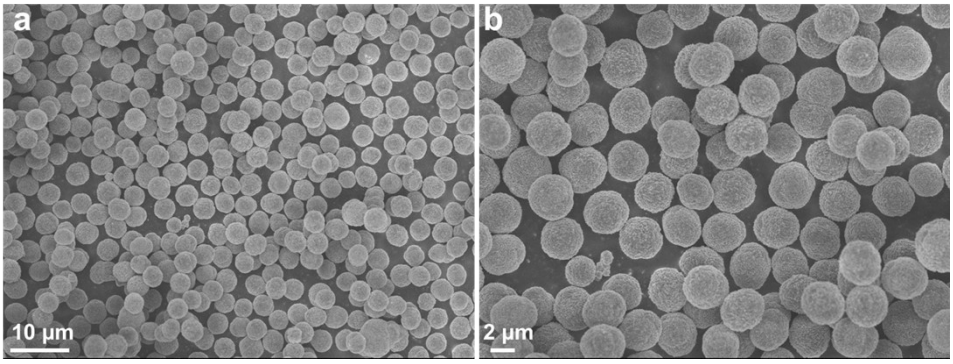

Figure S3. (a-b) SEM images of Mn_2O_3 sphere.

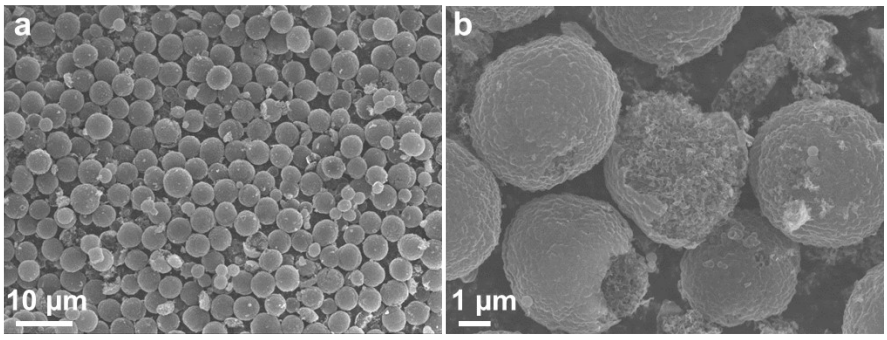

Figure S4. SEM images of carbon sphere.

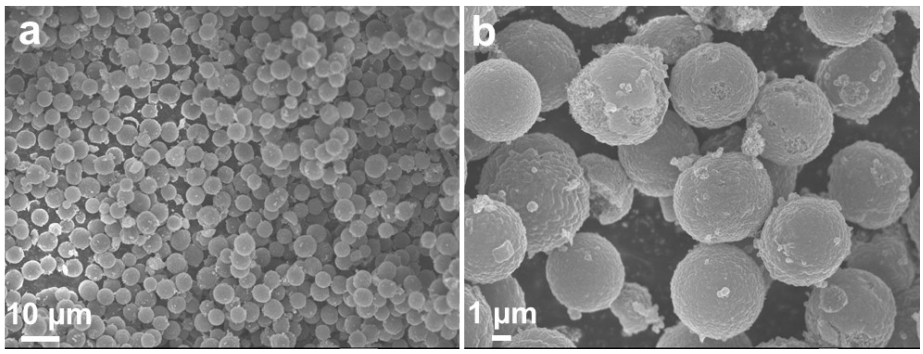

Figure S5. SEM images of Mo_2C/C.

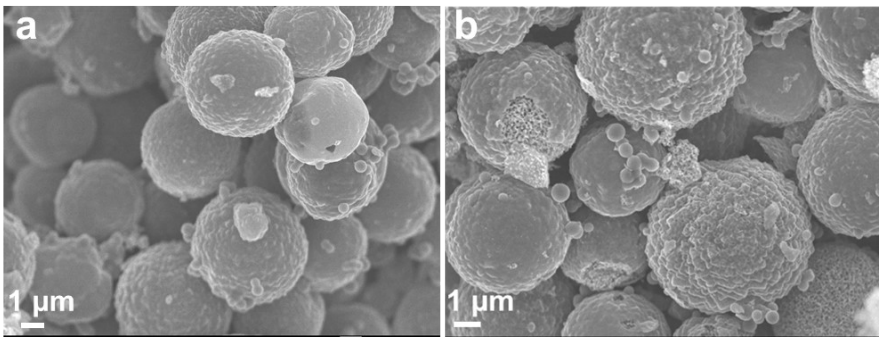

Figure S6. SEM images of S@Mo_2C/C.

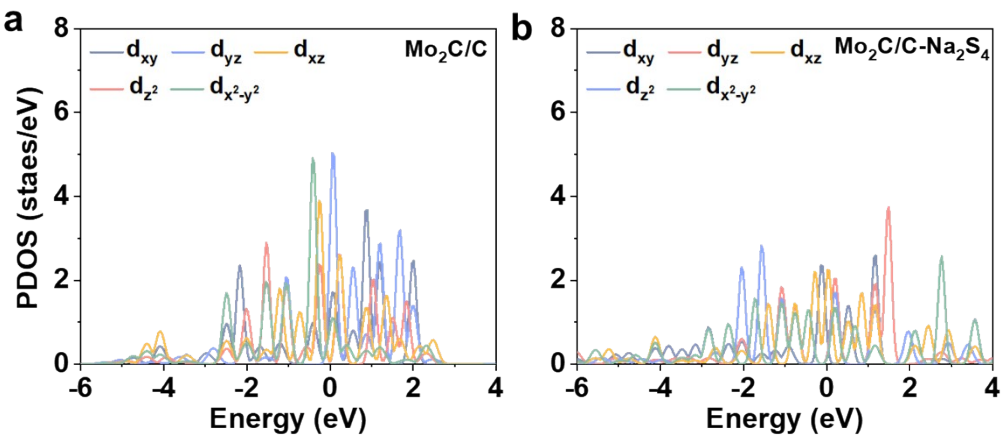

Figure S7. The PDOS of d orbital of (a) Mo_2C/C and (b) $Mo_2C/C\text{-}Na_2S_4$.

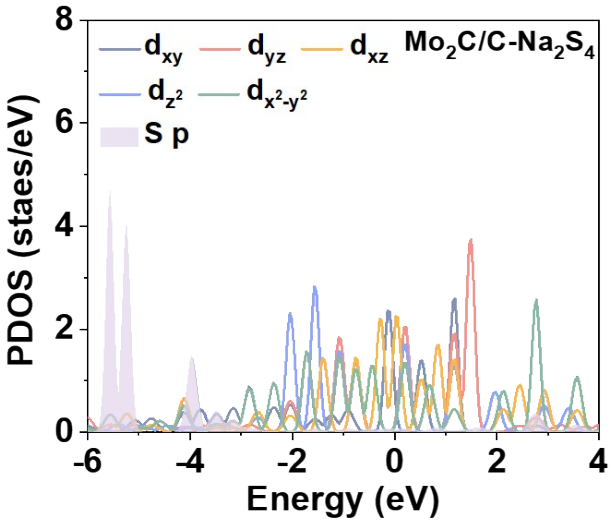

Figure S8. The PDOS of d orbital of Mo_2C/C and S p orbital of Na_2S_4 after Na_2S_4 adsorption.

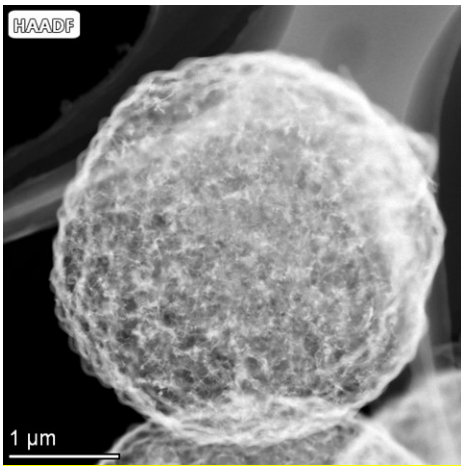

Figure S9. HAADF-STEM image of $S@Mo_2C/C$.

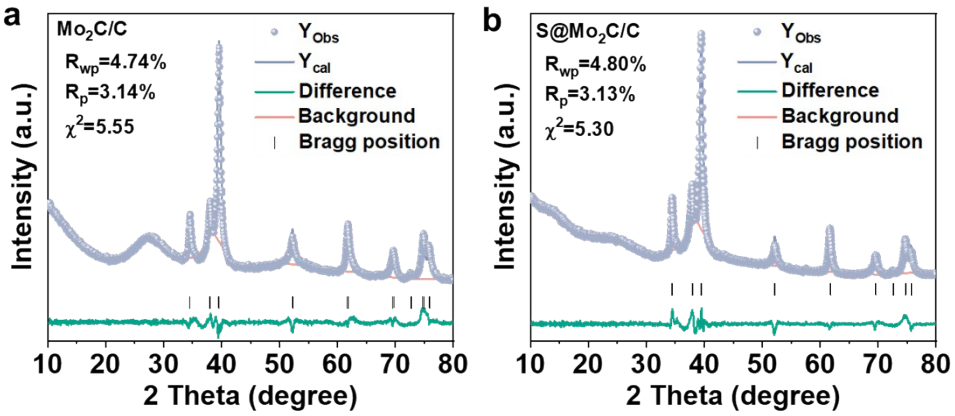

Figure S10. Rietveld refined XRD patterns of (a) Mo_2C/C and (b) $S@Mo_2C/C$.

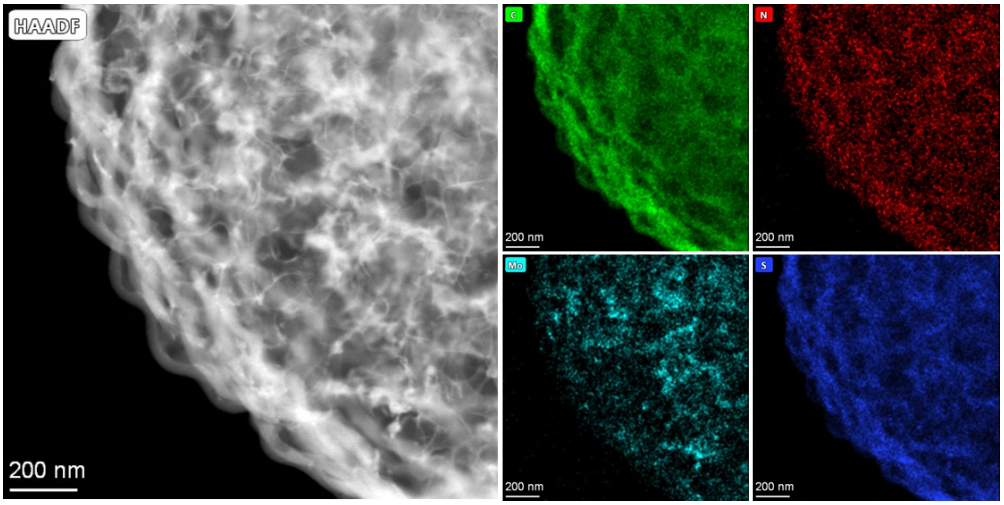

Figure S11. HAADF-STEM image and corresponding elemental mapping images of $S@Mo_2C/C$.

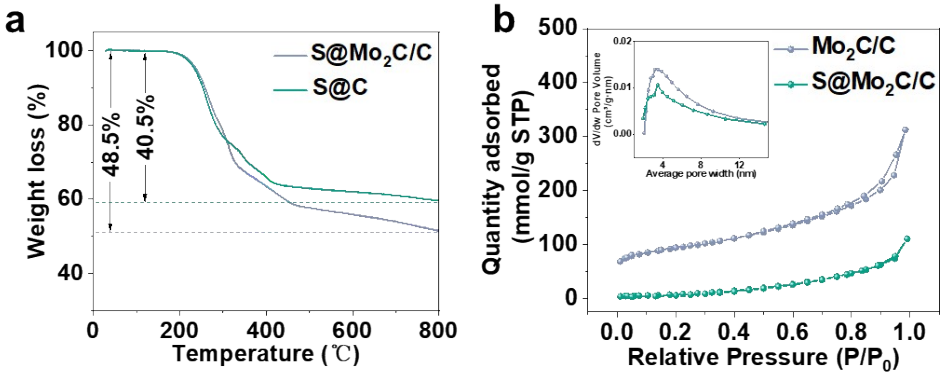

Figure S12. (a) Thermogravimetric (TG) profiles of $S@Mo_2C/C$ and S@C. (b) N_2 adsorption/desorption isotherms; inset shows the pore volumes.

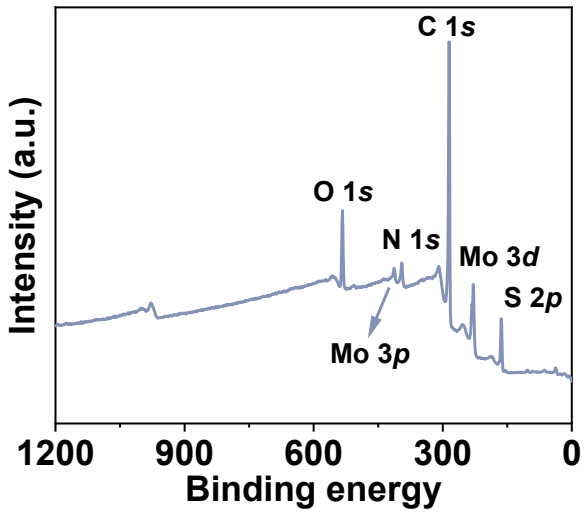

Figure S13. Survey XPS spectrum of S@Mo_2C/C.

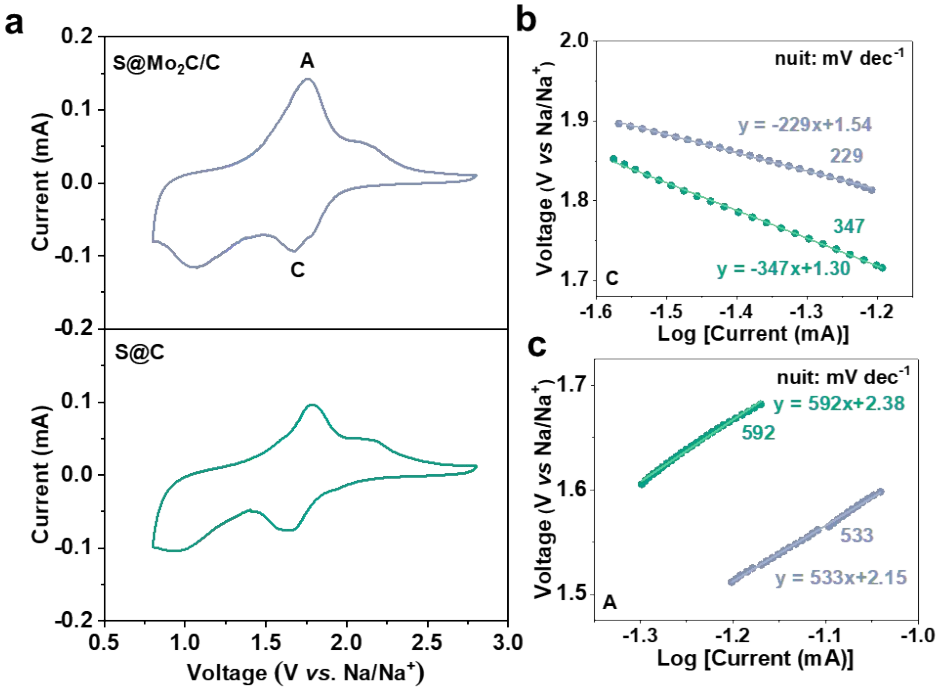

Figure S14. (a) CV curves of S@Mo_2C/C and S@C. (b-c) Tafel plots of S@Mo_2C/C and S@C as noted in (a) for the first cathodic reduction and anode oxidation process.

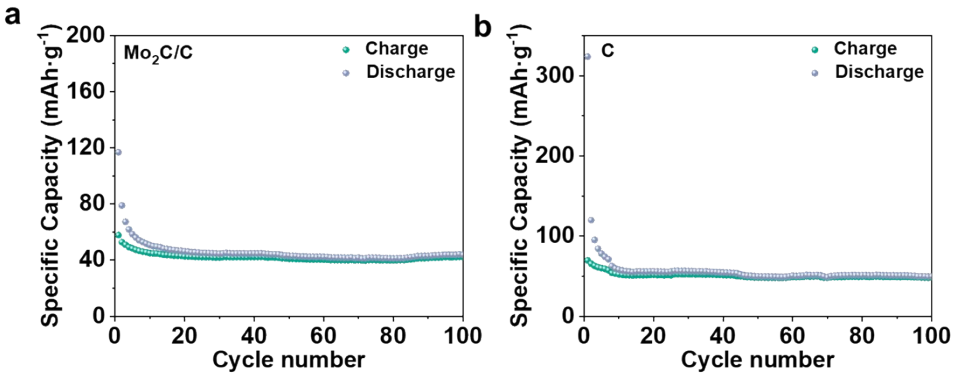

Figure S15. Cycling performance of (a) Mo_2C/C and (b) C at 200 mA g^{-1}.

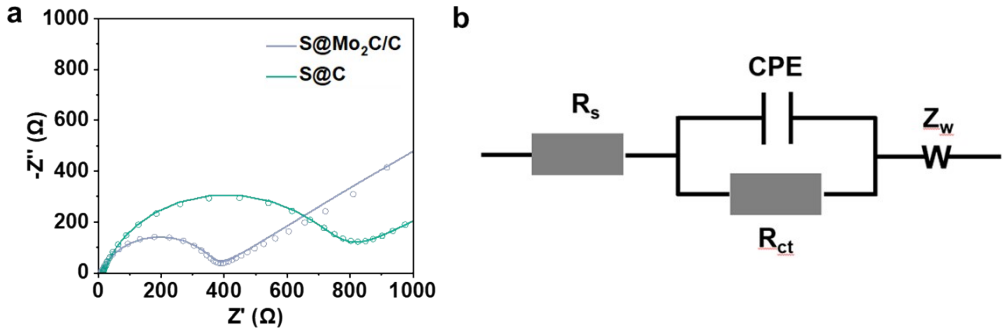

Figure S16. (a) Nyquist plots of S@Mo2C/C and S@C. (b) Equivalent circuit model.

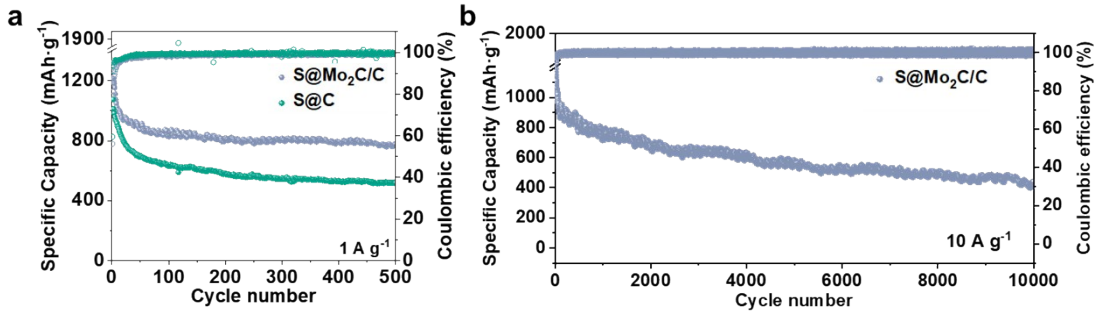

Figure S17. (a) Cycling performance of S@Mo2C/C at 1 A g^{-1}. (b) Long-term cycling performance of S@Mo2C/C at high rate of 10 A g^{-1}.

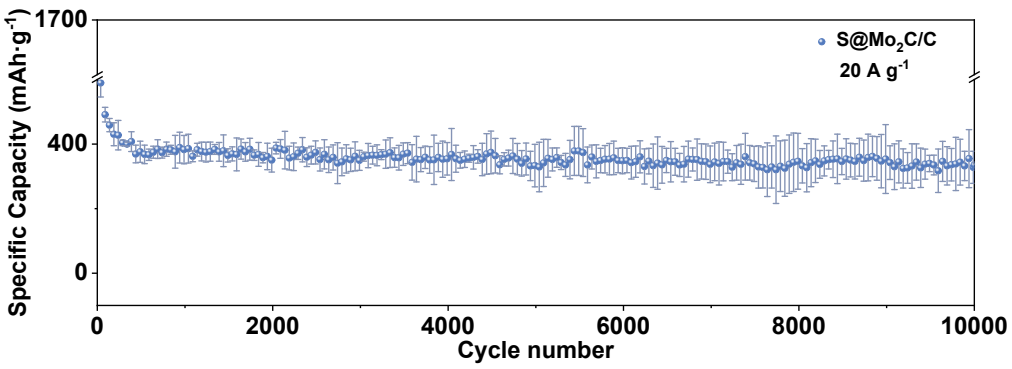

Figure S18. Cycling performance of S@Mo2C/C cathode with error bars at 20 A g^{-1}.

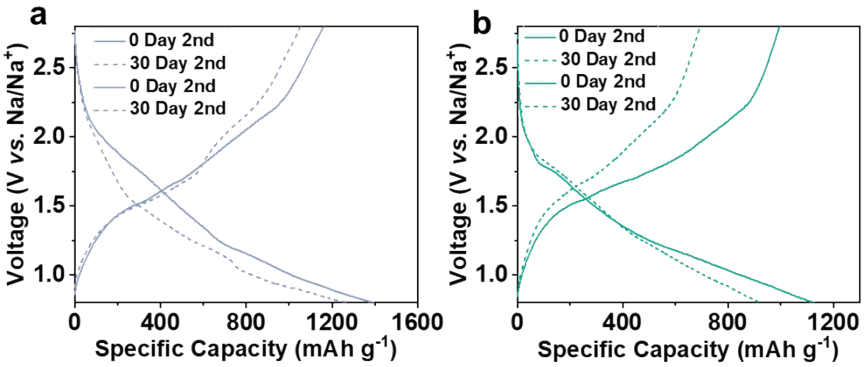

Figure S19. Galvanostatic charge-discharge (GCD) curves of (a) S@Mo_2C/C, and (b) S@C with different rest time.

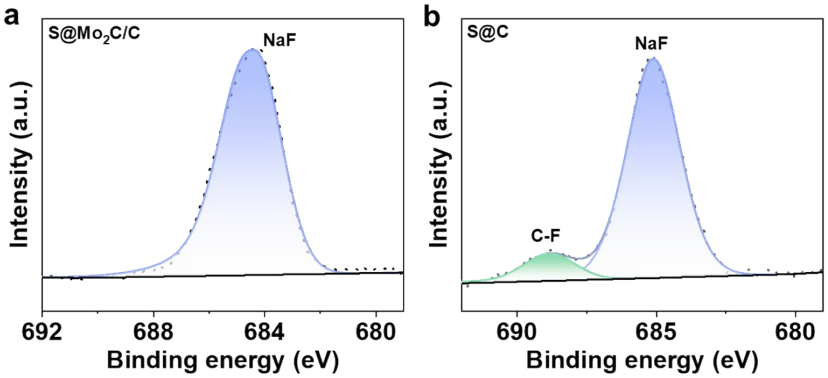

Figure S20. XPS spectra of F 1*s* of Na metal anodes from (a) S@Mo_2C/C and (b) S@C after three cycles.

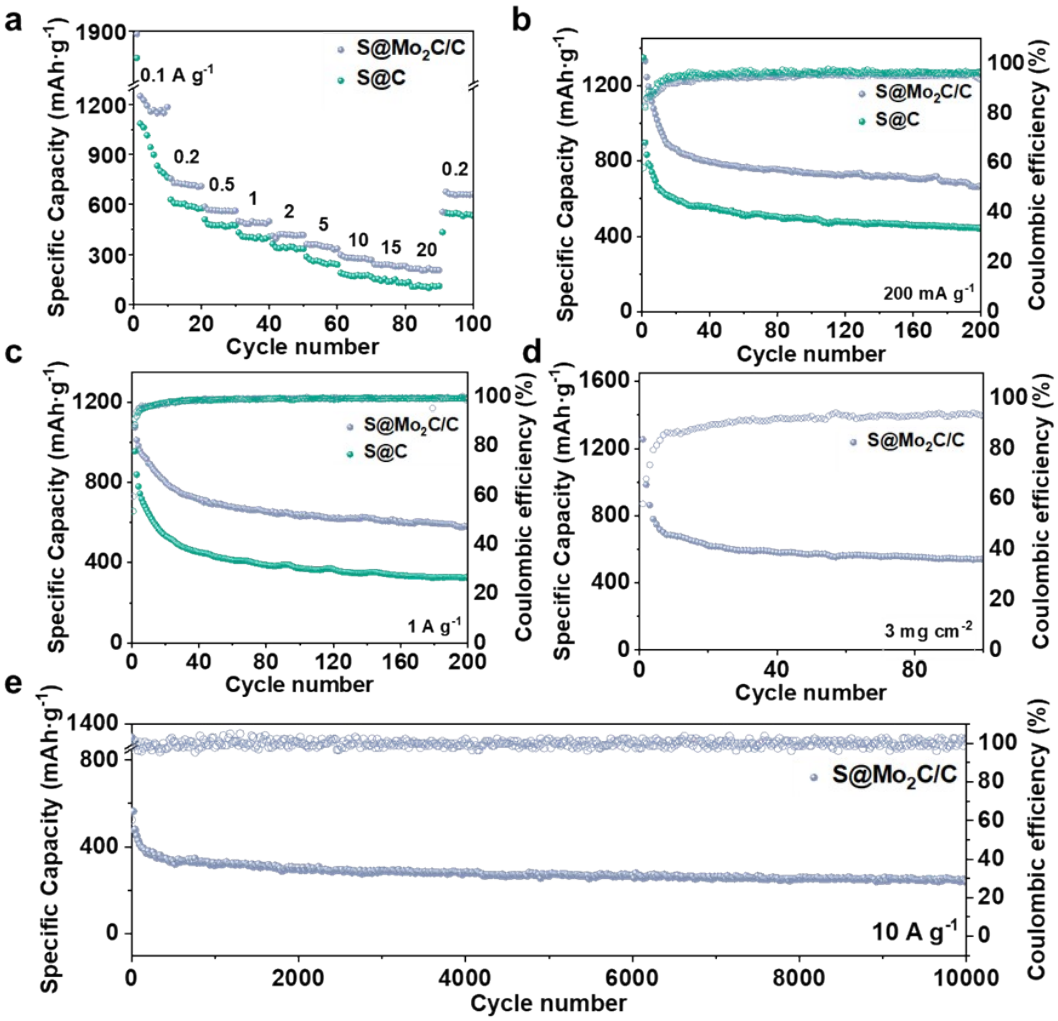

Figure S21. (a) Rate performance of S@Mo2C/C and S@C with sulfur loading of ~1.2 mg cm^{-2}. (b) Cycling performance at 200 mA g^{-1} with sulfur loading of ~1.2 mg cm^{-2}. (c) Cycling performance at 1 A g^{-1} with sulfur loading of ~1.2 mg cm^{-2}. (d) Cycling performance at 200 mA g^{-1} with sulfur loading of ~3 mg cm^{-2}. (e) Long-term cycling performance of S@Mo2C/C at high rate of 10 A g^{-1} with sulfur loading of ~1.2 mg cm^{-2}.

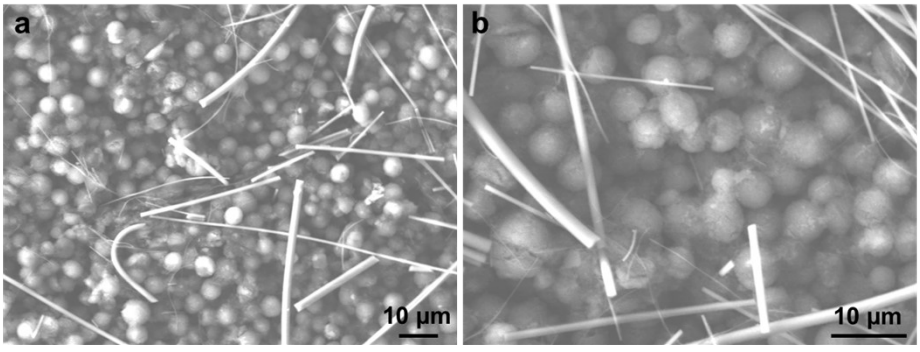

Figure S22. SEM images of (a) S@Mo$_2$C/C cathode and (b) S@C cathode after 100 cycles at 1 A g^{-1}.

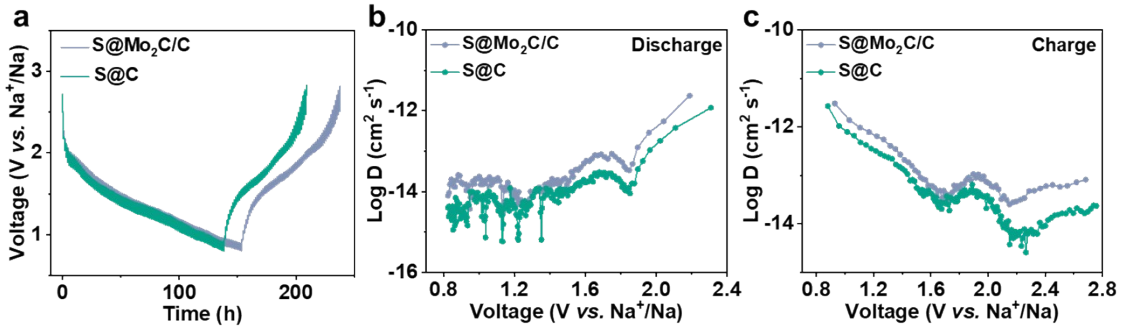

Figure S23. (a) Galvanostatic intermittent titration technique (GITT) curves of S@Mo_2C/C and S@C cathodes for Na-S batteries. (b-c) The Na-ion diffusion coefficient during the discharging process and charging process.

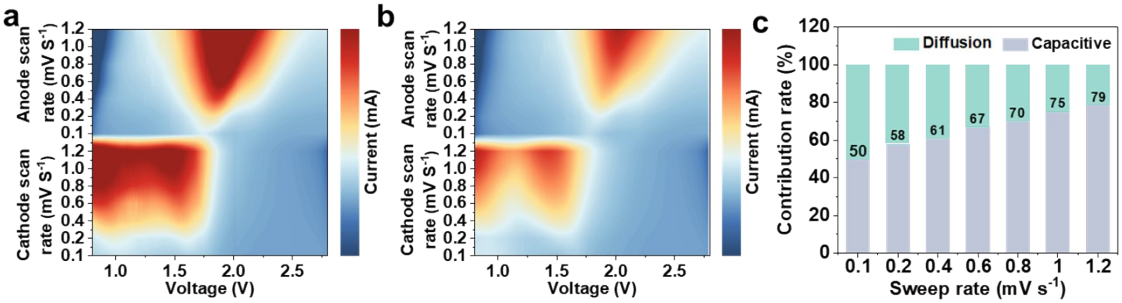

Figure S24. (a) Contour plots of CV patterns of S@Mo2C/C. (b) Contour plots of CV patterns of S@C. (c) The ratios of capacitive/diffusion contributions in S@Mo2C/C under various scan rates.

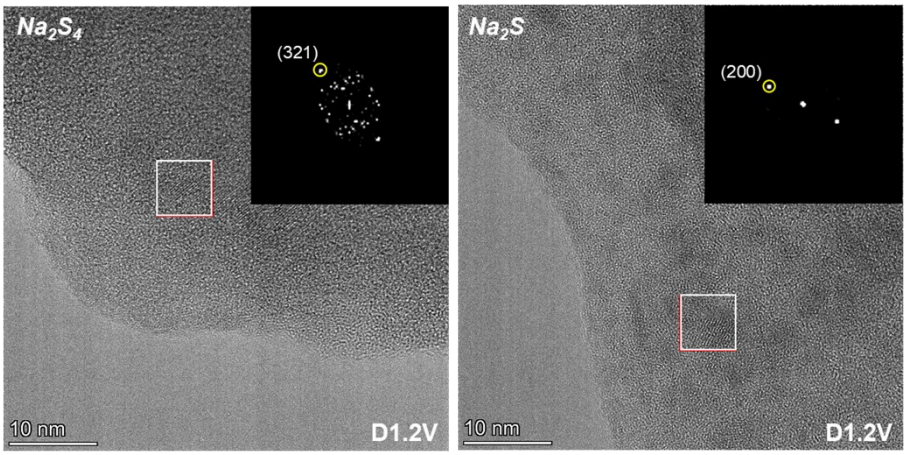

Figure S25. *Ex situ* HRTEM images with the corresponding fast Fourier transform (FFT) patterns at discharge of 1.2 V in the first cycle.

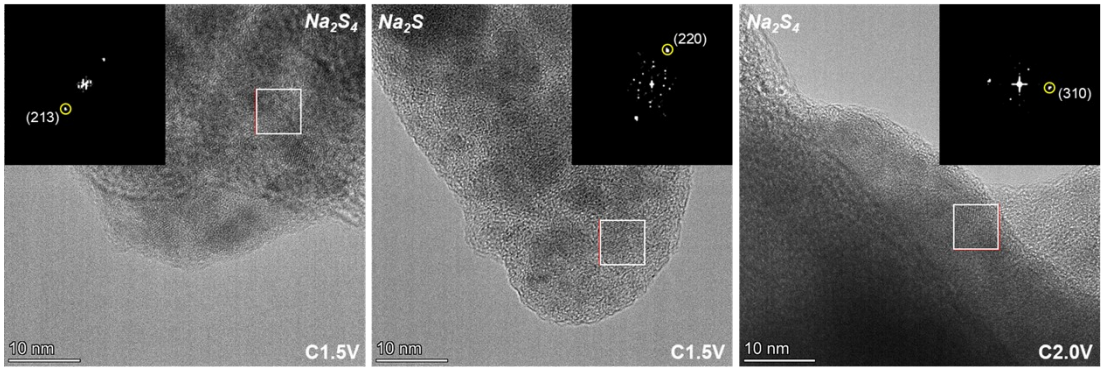

Figure S26. *Ex situ* HRTEM images with the corresponding FFT patterns at charge of 1.5 V and 2.0 V in the first cycle.

Table S1. Quantitative EXAFS fitting results of Mo_2C/C and S@Mo_2C/C.

Sample	Scattering path	Distance (Å)	C.N.	σ^2 (Å^2)	ΔE_0 (eV)
Mo_2C/C	Mo-C	2.13	2.1	0.005	-3.1
	Mo-Mo	2.97	4.9	0.005	-3.1
S@Mo_2C/C	Mo-C	2.11	2.24	0.004	0.716
	Mo-S	2.43	0.75	0.004	0.716
	Mo-Mo	2.99	3.60	0.004	0.716

S_0^2 of Mo=0.8

Fourier transform of k range is 3-12 Å^{-1}.

Refernce

1. N. Wang, Y. Wang, Z. Bai, Z. Fang, X. Zhang, Z. Xu, Y. Ding, X. Xu, Y. Du and S. Dou, *Energy Environ. Sci.*, 2020, **13**, 562-570.
2. G. Kresse and J. Hafner, *Phys. Rev. B*, 1993, **47**, 558-561.
3. G. Kresse and J. Hafner, *Phys. Rev. B*, 1994, **49**, 14251-14269.
4. P. E. Blöchl, *Phys. Rev. B*, 1994, **50**, 17953-17979.
5. G. Kresse and D. Joubert, *Phys. Rev. B*, 1999, **59**, 1758-1775.
6. J. P. Perdew, K. Burke and M. Ernzerhof, *Phys. Rev. Lett.*, 1996, **77**, 3865-3868.
7. V. Wang, N. Xu, J.-C. Liu, G. Tang and W.-T. Geng, *Comput. Phys. Commun.*, 2021, **267**, 108033.